Operational modal analysis of a ten-storey building featuring vertical modes

Zuo Zhu[a], Xinrui Wang[b], Siu-Kui Au[c], Yan-Long Xie[d*], James Brownjohn[a, e]

[a] Vibration Engineering Section, Faculty of Environment, Science and Economy, University of Exeter, Exeter, UK

[b] School of Civil Engineering and Built Environment, Liverpool John Moores University, UK

[c] School of Civil and Environmental Engineering, Nanyang Technological University, Singapore

[d] College of Civil and Transportation Engineering, Shenzhen University, Shenzhen, Guangdong 518060, China

[e] Full Scale Dynamics Ltd, The Innovation Centre, Sheffield, UK

* Corresponding author. E-mail: yanlongxie@szu.edu.cn

Abstract

As a contribution to addressing challenges and improving technology in field implementation and practice of 'operational modal analysis' (OMA), a vibration test was carried out on a ten-storey rectangular building, featuring modal identification for both horizontal and vertical axes over a grid of 80 locations. The study used six triaxial accelerometers in 20 setups and the particular challenges with data are with close/buried modes, significant noise disparity, and contamination with harmonic signals in two frequency bands around 2 Hz and 8 Hz, which are addressed using recently developed techniques in Bayesian OMA. A particular feature of the building dynamic behaviour in the higher band of modes revealed by the study was a set of global vertical vibration modes. In addition to the short-term multi-setup test, two months of monitoring data were collected using a single accelerometer on the top floor to study amplitude dependence and ensemble statistics of modal properties, particularly for the first horizontal mode. The results reveal that the natural frequencies of the first three modes decrease with the

vibration level while the damping of the first mode shows an increasing trend. The field data used in this study are archived in an open repository for public access.

Keywords: Ambient vibration test; operational modal analysis; vertical modes; buried modes; multiple setups; BAYOMA

1 Introduction

Full-scale vibration testing has become an indispensable tool for in-situ update and monitoring of structural modal properties (MPs) i.e., natural frequencies, damping ratios and mode shapes. MPs provide information for downstream applications, e.g., vibration diagnosis/control [1], model updating [2], damage detection [3] and structural health monitoring [4,5]. Although forced vibration (known input) tests can yield more accurate estimates of MPs, the ambient vibration test (AVT) has become popular for its simplicity in implementation, thanks to advances in theory and instrumentation technology. An increasing number of AVTs have been carried out in the last few decades, e.g., bridges [6], buildings [7], lighthouses [8], telecoms structures [9] and wind turbines [10].

Performed under a complex field environment that is not repeatable, every field test is unique, presenting potential challenges that demand continuing research effort. Structures under operational conditions are mainly excited by wind, micro tremors, traffic and human activities and for buildings the levels of ambient vibration testing without coincidental timing of strong tremors or storms are generally much lower than that of bridges due to their relatively high mass/load ratio. As a result, sensors for vibration tests of buildings need to have much lower self-noise, usually in the order of $1\ \mu\text{g}/\sqrt{\text{Hz}}$, for good quality data.

A salient feature of the present study is detailed identification of a set of vertical vibration modes. Global ambient vertical vibrations in buildings are generally weak compared to horizontal motion in sway and torsion and their MPs are seldom studied in the literature. The exception is forced vibration testing of floor slabs in relation to vibration serviceability under footfall excitation. In fact, such shaker tests of floors have often revealed apparent global modes with clear but relatively weak column vertical motion [11] and high modal mass, and these modes can potentially enhance vertical ground-borne vibration originating from blasting [12] and vehicles via mode shapes with ordinates increasing with storey level. Accessible studies on global vertical MPs include use of seismic response records to identify the 1.87 Hz first vertical mode of a 52-storey building [13] and a study of a 39-storey building in Korea (2011) that experienced vertical shaking resulting in an emergency evacuation. A subsequent field investigation [14] revealed a suspected linkage to a global vertical mode at 2.7 Hz, which is near the frequency of human group rhythmic movements.

Contributing to field implementation and practice of operational modal analysis (OMA), this work presents the ambient vibration test of the ten-storey Roxby building, capturing both horizontal and vertical vibration responses using a set of six triaxial accelerometers. There were specific challenges in the AVT and the subsequent modal identification, using twenty setups across two days to recover high-resolution mode shapes at 80 locations. Performing modal identification with a large number of setups is a challenging task due to the non-stationary environmental conditions. Depending on the sensor locations and excitation levels (which cannot be controlled), a structural mode that exhibits high modal signal-to-noise ratio in one setup could be 'buried' by the vibration response in directions irrelevant to this mode in another setup, posing challenges in identifying the 'global mode shapes' covering all the measured degrees of freedom. A second challenge is harmonic signals (from machinery in or around the building) in the measured data. In OMA, the excitation is assumed to be broadband random, but since the excitation cannot be actively controlled in AVT, such harmonic signals can contaminate the data. Mitigating this problem requires proper measures to be taken to avoid biased estimates especially when the frequencies of the harmonic signals are within the resonant bands of the modes of interest. These challenges are addressed using the recently developed techniques in Bayesian OMA.

Although there are several studies tracking modal properties of super-tall buildings during typhoon events in recent years [15–17], much less attention is paid to mid-rise buildings. Even for super-tall buildings, the relationship between the vibration level and damping ratios still remains unclear and there is no commonly accepted amplitude-dependent damping model. Unlike natural frequency, damping cannot be predicted from a structural model. Empirical models for damping are available in the literature [18,19]. The damping values used for deriving the models were often estimated using early OMA techniques (e.g., half-power bandwidth) and their reliability is questionable [20]. Contributing to the investigation of amplitude-dependent properties of modal parameters, acceleration on the top level of the building was monitored continuously for two months. Several strong wind events were captured, giving reliable data across different orders of vibration levels. MPs were tracked for these data using a recently developed Bayesian dynamic programming method [21] and potential amplitude-dependent properties of modal parameters are investigated. A prediction model of modal parameters is established, and it has the potential to be used for anomaly detection when new data are obtained in the future.

2 Description of the building

The Roxby building (Figure 1) is a reinforced concrete structure located on the campus of the University of Liverpool, comprising ten storeys above ground plus a basement, with a total height of approximately 40 metres and primarily housing offices and laboratories for the Department of Geography and Planning. It was constructed between 1961 and 1966 in the Brutalist style. Vertical loads are supported by a regular grid of reinforced concrete columns and deep spandrel beams integrated into the façade, with concrete slabs spanning between them.

Lateral stability is achieved through reinforced concrete shear walls located at the northwest and northeast corners, which primarily resist north-south lateral loads, and a substantial shear wall along the south façade, which resists east-west loading. These elements, together with the central stair and lift core and the stiff perimeter frame, form a continuous and efficient load path for both vertical and lateral forces. Figure 2 shows the plan view of a typical floor below Level 8, where two rows of columns are arranged along the corridor between the stairwell and the lift core and the rectangular floor slab spans over a $32 \times 13\ \mathrm{m}^2$ area. The layouts of Levels 9 and 10 differ from the lower floors, featuring only a single row of columns in this area (Figure 3). The sensor locations indicated in Figure 2 are discussed in Section 3.

Figure 1 Roxby building.

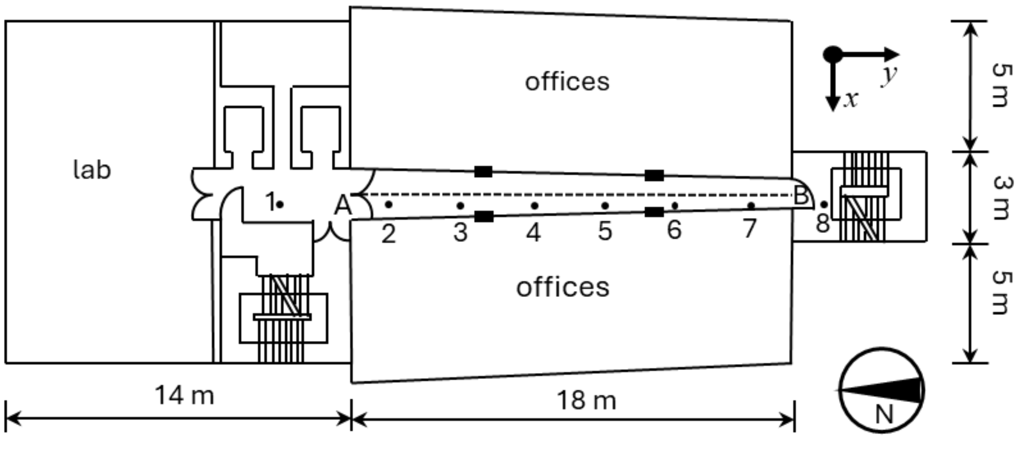

Figure 2 Typical floor plan below Level 8. Dot – test point; black box – column.

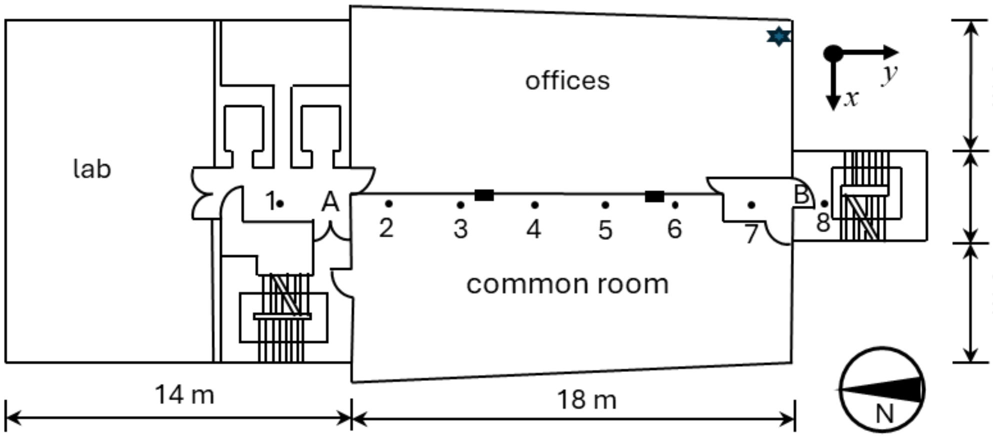

Figure 3 Typical floor plan at Level 10. Dot – test point; black box – column; star – monitoring location.

3 Instrumentation

A total of six accelerometers were available for the vibration testing of the building. Figure 4(a) shows one set of equipment which comprises an accelerometer, GPS receiver, high-precision clock, battery and cables. The accelerometer (Guralp 5TDE) is a three-axis force-balance accelerometer packaged together with a 24-bit digitiser, an embedded Linux-based acquisition module and an onboard storage unit. It has a maximum measurement range of $\pm 2\mathrm{g}$ and a sampling rate ranging from 1 Hz to 1000 Hz. The noise level of the sensor is $< 1\ \mu\mathrm{g}/\sqrt{\mathrm{Hz}}$ estimated based on a 'huddle test' method [22], which is well below the ambient vibration level of civil structures in urban areas, so adequate signal-to-noise (s/n) ratios would be expected in this application. The battery is of lithium polymer type with a minimum capability of 16 Ah and can power continuous operation of the equipment for at least two days on a full charge. Sensor specification is summarised in Table 1.

Table 1 Sensor specification

Parameters	Value
Acceleration range	$\pm 2\mathrm{g}$
Self-noise	$< 1\ \mu\mathrm{g}\ /\ \sqrt{\mathrm{Hz}}$
Digitiser resolution	24-bit
Dynamic range	135 dB
Maximum sample rate	1000 Hz

Timing sources	GPS; external high-precision clock
Power supply voltage	11-30 V DC

Figure 4 (a) A set of equipment used in the field test; (b) ‘huddle test’ by placing sensors together to check the status of the instruments; (c) on-site view of the equipment.

Due to requirements of the subsequent modal analysis, data acquired by multiple sensors used in vibration tests must be synchronous, i.e., recorded simultaneously at the same time scale. Depending on the site conditions, there are two means to synchronise this type of sensor. Because these sensors do not use a wired central data acquisition system, for outdoor measurements (e.g., bridges), sensors are synchronised through GPS receivers with common time signals from satellites. For indoor applications (e.g., in the current test), where GPS receivers cannot receive signals without a clear view of the sky, high-precision clocks are used, having been initially synchronised and trained using GPS receivers at a place with a clear view of the sky. Once the clocks are locked, the GPS receivers can be disconnected so the clocks can then be transported to the deployment site and connected to the sensors to provide timing information. The accuracy of the high-precision clock used here is 0.038 ppm (parts per million), giving a relative drift of $2 \times 0.038 \times 10^{-6} \times 3600 \times 8 \approx 2$ ms over 8 hours. For a single 10 Hz mode, the phase shift caused by a 2 ms time error would be $2\pi \times 10 \times 0.002 = 7.2°$, leading to a relative mode shape error of $1 - \cos 7.2° = 0.79\%$. Such error is small enough to be negligible in OMA.

Test locations

Since the laboratories and offices were not accessible, the test locations were arranged along the corridors on the south side of the building, as shown in Figure 2, providing triaxial measurement at 8 'test points' (TPs) on each floor, generally spaced 3 m apart. Such spacing is expected to give high spatial resolution in the identified mode shapes, enabling the evaluation of potential structural issues. TP 1 is located slightly further (about 5 m) from TP 2 to avoid disturbing building occupants near the lift lobby door. In total, $10 \times 8 = 80$ TPs were measured, giving $80 \times 3 = 240$ measured degrees of freedom (DOFs) over all three axes.

Sensor alignment

It was intended to obtain mode shapes with all TPs within the same vertical plane. Sensor alignment is very important in vibration tests as it directly affects the quality of identified mode shapes. Physical features (e.g., walls, columns) are commonly used to provide references for sensor alignment. However, in the current study, it was not straightforward to align all the sensors based on a common physical feature (e.g., walls). The wall beside TP 1 is not parallel to that beside TPs 2-7 and TP 8 located in a stairwell is not close to any of walls. On the other hand, the layout of Levels 9 and 10 is different from that of lower floors. The corridor becomes narrower on Level 9 and hence the location of the walls along the corridor differs from that of the lower floors in the floor plan. There is no corridor in Level 10 and a single wall separated the floor into two large social spaces. The solution to the alignment challenges was to mark a line across the centre of Doors A and B on each floor as the reference (See Figure 2) since drawings indicate that these lines on different floors lie within the same vertical plane. The north channel of each sensor was oriented along the line towards Door B with an offset of 35 cm from the reference lines to reduce the risk of disturbing the building users.

Reference sensors and roving setups

Having more TPs (80) than sensors (6) requires test planning with multiple setups, with each setup covering different parts of the structure while sharing sufficient common reference DOFs. Determining the reference DOFs and their corresponding TPs is a critical aspect in the planning of multiple setups. In order to assemble 'local mode shapes' in different setups into 'global mode shapes' covering all the measured DOFs, the reference DOFs should contain sufficient modal information on all the modes of interest. In this test, it was decided to have two reference sensors on the top level of the building, one at TP 1 and the other at TP 8 (total 6 DOFs), because the top level usually has large vibration responses and having two reference sensors (rather than one) can effectively avoid the situation where a single reference TP is at the node of a mode. The remaining four sensors were 'roved' from the top to the ground floor in different setups. At each floor, TPs 1, 3, 5 and 7 were first measured, followed by TPs 2, 4, 6 and 8. In total, 20 setups were conducted to cover all the TPs of interest.

Before the multiple setup test, a reconnaissance measurement with a single accelerometer on the top floor found the fundamental mode to have a natural frequency of around 2 Hz. Based on this, setup duration was set at 10 minutes, giving around $600 \times 2 = 1200$ cycles of the fundamental mode, which is typically long enough for reliable estimations based on 'uncertainty laws' [23].

The multiple setup test was carried out on 15 November 2018 with sensors synchronised using high-precision clocks due to a weak GPS signal inside the building. The sensor sampling rate was set at 100 Hz, which is considered sufficiently high to accurately capture the dynamic behaviours of interest while avoiding excessively high data volumes that would impose unnecessary storage and processing demands. A 'huddle test' was performed before the setups by co-locating all the sensors at a TP on the top floor, see Figure 4(b), enabling checking of sensor status on-site, e.g., synchronisation and channel noise. It was only possible to make measurements in the afternoon of 15 November, with the first fifteen setups completed before the building closed at 5 pm; Figure 4(c) shows one set of equipment during these setups. The remaining five setups were performed on 26 November 2018.

4 Modal identification

Consider a classically damped N-degree-of-freedom structure system with the mass, damping and stiffness matrices being respectively denoted by $\boldsymbol{M}, \boldsymbol{C}$ and $\boldsymbol{K}$. The equation of motion can be expressed as

$$\boldsymbol{M}\ddot{\boldsymbol{x}}(t) + \boldsymbol{C}\dot{\boldsymbol{x}}(t) + \boldsymbol{K}\boldsymbol{x}(t) = \boldsymbol{w}(t) \tag{1}$$

where $\boldsymbol{x}(t)$, $\dot{\boldsymbol{x}}(t)$ and $\ddot{\boldsymbol{x}}(t)$ are the $N \times 1$ displacement, velocity and acceleration response vectors, respectively; $\boldsymbol{w}(t)$ is the excitation force vector. The natural frequencies $\{\omega_i\}_{i=1}^N$ (rad/s) and mode shapes $\{\boldsymbol{\psi}_i\}_{i=1}^N$ can be obtained by solving the eigenvalue problem $\boldsymbol{K}\boldsymbol{\psi}_i = \omega_i^2 \boldsymbol{M}\boldsymbol{\psi}_i$. The response is then given by the sum of modal contributions $\boldsymbol{x}(t) = \sum_{i=1}^N \boldsymbol{\psi}_i \eta_i(t)$ where $\{\eta_i(t)\}_{i=1}^N$ are the modal response, each satisfying its own single-degree-of-freedom equation of motion:

$$\ddot{\eta}_i(t) + 2\zeta_i\omega_i\dot{\eta}_i(t) + \omega_i^2\eta_i(t) = p_i(t) \quad i = 1, \ldots, N \tag{2}$$

where ζ_i and $p_i(t)$ are respectively the modal damping ratio and modal force of the $i-th$ mode and they are defined such that $2\zeta_i\omega_i = \boldsymbol{\psi}_i^T\boldsymbol{C}\boldsymbol{\psi}_i \,/\, \boldsymbol{\psi}_i^T\boldsymbol{M}\boldsymbol{\psi}_i$ and $p_i(t) = \boldsymbol{\psi}_i^T\boldsymbol{w}(t) \,/\, \boldsymbol{\psi}_i^T\boldsymbol{M}\boldsymbol{\psi}_i$.

In OMA, the structural response is typically measured at a limited number of locations under ambient, noncontrollable, and immeasurable excitations. The objective of OMA is to identify structural modal properties such as natural frequencies, damping ratios and mode shapes based on the measured response only. Various OMA methods have been developed [24]. In this work, a Bayesian OMA (BAYOMA) approach [25,26] is applied to identify the modal parameters of the instrumented building as it provides a fundamental means to process the information in data and quantify the identification uncertainty. Operating in the frequency domain, BAYOMA makes use of the FFTs within the selected frequency bands around the subject modes to infer the modal properties [27]. Given the data, BAYOMA models the modal parameters as random variables which can be approximated with a Gaussian probability distribution with mean being the most probable value and standard deviation describing identification uncertainty. The theory of multiple-setup BAYOMA is briefly reviewed in this section.

Let $\left\{\hat{\ddot{\boldsymbol{x}}}_j^{(r)}\right\}_{j=0}^{N_r-1}$ $(n_r \times 1)$ denote the measured acceleration data at n_r DOFs in Setup r where N_r is the number of data samples per channel. Its scaled FFT at frequency $\mathrm{f}_k^{(r)} = k \,/\, N_r \Delta t_r$ is defined as $\hat{\boldsymbol{\mathcal{F}}}_k^{(r)} = \sqrt{2\Delta t_r / N_r} \sum_{j=0}^{N_r-1} \hat{\ddot{\boldsymbol{x}}}_j^{(r)} e^{-2\pi \mathbf{i} jk/N_r}$ where $\mathbf{i}^2 = -1$ and Δt_r is the sampling interval in Setup r. Suppose within the selected frequency band there are m dominated vibration modes following linear classically damped dynamics, $\hat{\boldsymbol{\mathcal{F}}}_k^{(r)}$ is modelled as

$$\hat{\boldsymbol{\mathcal{F}}}_k^{(r)} = \boldsymbol{\Phi}_r \boldsymbol{\eta}_k^{(r)} + \boldsymbol{\varepsilon}_k^{(r)} \tag{3}$$

where $\boldsymbol{\Phi}_r = [\boldsymbol{v}_{r1}, \ldots, \boldsymbol{v}_{rm}] \in R^{n_r \times m}$ with the $i-th$ column being the 'local mode shape' of the $i-th$ mode covering the measured DOFs in Setup r only; $\boldsymbol{\eta}_k^{(r)}$ is the scaled FFT of modal response at frequency $\mathrm{f}_k^{(r)}$; $\boldsymbol{\varepsilon}_k^{(r)} \in C^{n_r \times 1}$ denotes the scaled FFT of prediction error, assumed to be independent and identically distributed (i.i.d.) among different DOFs with a common power spectral density (PSD) $S_e^{(r)}$ within the band. By taking the scaled FFT on both sides of (2), it can be shown that $\boldsymbol{\eta}_k^{(r)} = \boldsymbol{h}_k^{(r)} \boldsymbol{p}_k^{(r)}$ where $\boldsymbol{h}_k^{(r)}$ is a diagonal matrix with the $i-th$ entry $h_{ik}^{(r)}$ being the frequency response function corresponding to Mode i; $h_{ik}^{(r)} = \left(1 - \beta_{ik}^{(r)2} - 2\zeta_i^{(r)} \beta_{ik}^{(r)} \mathbf{i}\right)^{-1}$ (for acceleration data) where $\beta_{ik}^{(r)} = f_i^{(r)} \,/\, \mathrm{f}_k^{(r)}$; $f_i^{(r)}$ and $\zeta_i^{(r)}$ are the natural frequency and damping ratio of Mode i in Setup r, respectively; $\boldsymbol{p}_k^{(r)} = \left[p_{1k}^{(r)}; \ldots; p_{mk}^{(r)}\right] \in C^{m \times 1}$ with $p_{ik}^{(r)}$ being the scaled FFT of the modal force at frequency $\mathrm{f}_k^{(r)}$ and they are assumed to be stationary with a constant PSD matrix $\boldsymbol{S}^{(r)} \in C^{m\times m}$ within the selected frequency band (so only band-limited white).

In a multiple-setup test, the main objective is to obtain the 'global mode shapes' covering all the measured DOFs. Let $\boldsymbol{\varphi}_i$ $(n \times 1)$ denote the global mode shape of the i-th mode. It can be related to the local mode shape $\boldsymbol{v}_{ri}$ by a selection matrix $\boldsymbol{L}_r \in R^{n_r \times n}$, i.e., $\boldsymbol{v}_{ri} = \boldsymbol{L}_r \boldsymbol{\varphi}_i$ $(i = 1, \dots, m)$. The selection matrix $\boldsymbol{L}_r$ is defined such that the (j,k)-entry of $\boldsymbol{L}_r$ is 1 if the j-th data channel in Setup r measures the DOF k in $\boldsymbol{\varphi}_i$ and zero otherwise. In the above context, the modal properties $\boldsymbol{\theta}$ to be identified comprise $= \left\{\left\{\left\{f_i^{(r)}\right\}_{i=1}^{m}, \left\{\zeta_i^{(r)}\right\}_{i=1}^{m}, \boldsymbol{S}^{(r)}, S_e^{(r)}\right\}_{\boldsymbol{r}=1}^{n_s}, \boldsymbol{\Phi} = [\boldsymbol{\varphi}_1, \dots, \boldsymbol{\varphi}_m]\right\}$. BAYOMA makes use of the FFTs from multiple setups for inference. Using Bayes' theorem and assuming a uniform prior distribution for $\boldsymbol{\theta}$, the posterior probability density function (PDF) of $\boldsymbol{\theta}$ given the data FFTs $D = \left\{\left\{\widehat{\boldsymbol{\mathcal{F}}}_k^{(1)}\right\}, \dots, \left\{\widehat{\boldsymbol{\mathcal{F}}}_k^{(n_s)}\right\}\right\}$ is proportional to the likelihood function, i.e., $p(\boldsymbol{\theta}|D) \propto p(D|\boldsymbol{\theta})$. For long data, the FFTs D follow a (circular symmetric) complex Gaussian distribution and are independent at different frequencies and different setups. It can be shown that the negative of the log-likelihood function (NLLF) is given by [25]

$$\mathrm{L}(\boldsymbol{\theta}) = -\ln p(D|\boldsymbol{\theta}) = \sum_{r=1}^{n_s}\Big[n_r N_f^{(r)} \ln \pi + \sum_k \ln\left|\boldsymbol{E}_k^{(r)}\right| + \sum_k \boldsymbol{\mathcal{F}}_k^{(r)*} \boldsymbol{E}_k^{(r)-1} \boldsymbol{\mathcal{F}}_k^{(r)}\Big] \tag{4}$$

where $N_f^{(r)}$ is the number of FFT points in the selected frequency band in Setup r; '*' denotes the complex conjugate transpose; the sum inside the bracket is over all frequencies in the selected band;

$$\boldsymbol{E}_k^{(r)} = \boldsymbol{\Phi}_r \boldsymbol{H}_k^{(r)} \boldsymbol{\Phi}_r^{\mathrm{T}} + S_e^{(r)} \boldsymbol{I}_{n_r} \tag{5}$$

is the theoretical PSD of the data in Setup r with $\boldsymbol{H}_k^{(r)} = \boldsymbol{h}_k^{(r)}\boldsymbol{S}^{(r)}\boldsymbol{h}_k^{(r)*}$. By minimising the NLLF in (4) (equivalent to maximising the posterior PDF $p(\boldsymbol{\theta}|D)$), one can obtain the most probable value (MPV) of modal parameters. An efficient algorithm has been developed recently, see [25] for details. The identification uncertainty can be quantified in terms of the posterior covariance matrix of the modal parameters. Mathematically, it is equal to the inverse of the Hessian matrix of the NLLF at the MPV. Analytical expressions for the Hessian matrix have been derived in [26], allowing the identification uncertainty to be quantified accurately and efficiently. The algorithms have been validated through numerical, laboratory and field data in the previous work [25,26] and have been successfully applied to the modal identification of buildings [28] and bridges [29]. In this work, these algorithms [25,26] will be used to identify the modal parameters of the instrumented building and quantify the identification uncertainty.

5 High-resolution mode shape test

5.1 Spectra analysis

As mentioned in Section 3, Setups 1-15 and 16-20 were performed with a two-week interval. Figure 5(a) and (c) show the root PSD up to 10 Hz for the data collected in Setup 1 (the first testing day) and Setup 16 (the second testing day two weeks later) where the blue, green and red lines indicate the response along *x, y* and vertical directions, respectively. Clear peaks which are concentrated around 2 Hz and 8 Hz indicate the potential existence of structural modes. Figure 5(b) and (d) show the corresponding singular value (SV) spectrum (i.e., eigenvalues of the real part of the PSD matrix versus frequency), where the number of distinctly higher lines indicates the number of modes within the band. From Figure 5(b), there are three lines (blue, red and yellow) significantly above the remaining ones around 2 Hz, indicating the presence of three modes in this region. The second and third modes are closely spaced, with overlapping resonant bands, but are clearly distinguishable from the first mode. These three modes feature with high modal s/n ratios. The fourth and fifth maximum eigenvalues (green and purple lines) in the SV spectrum of Setup 16 (Figure 5(d)) show slight elevations around 2 Hz compared to the noise level, a trend also observed in other setups conducted on the second testing day. This is due to the slight synchronisation errors among the high-precision clocks, arising during the initial training by GPS receivers. Based on the authors' experience, the effect of such small timing errors (a few milliseconds) can be neglected when one is concerned with the activities at low frequency range (say, < 10 Hz).

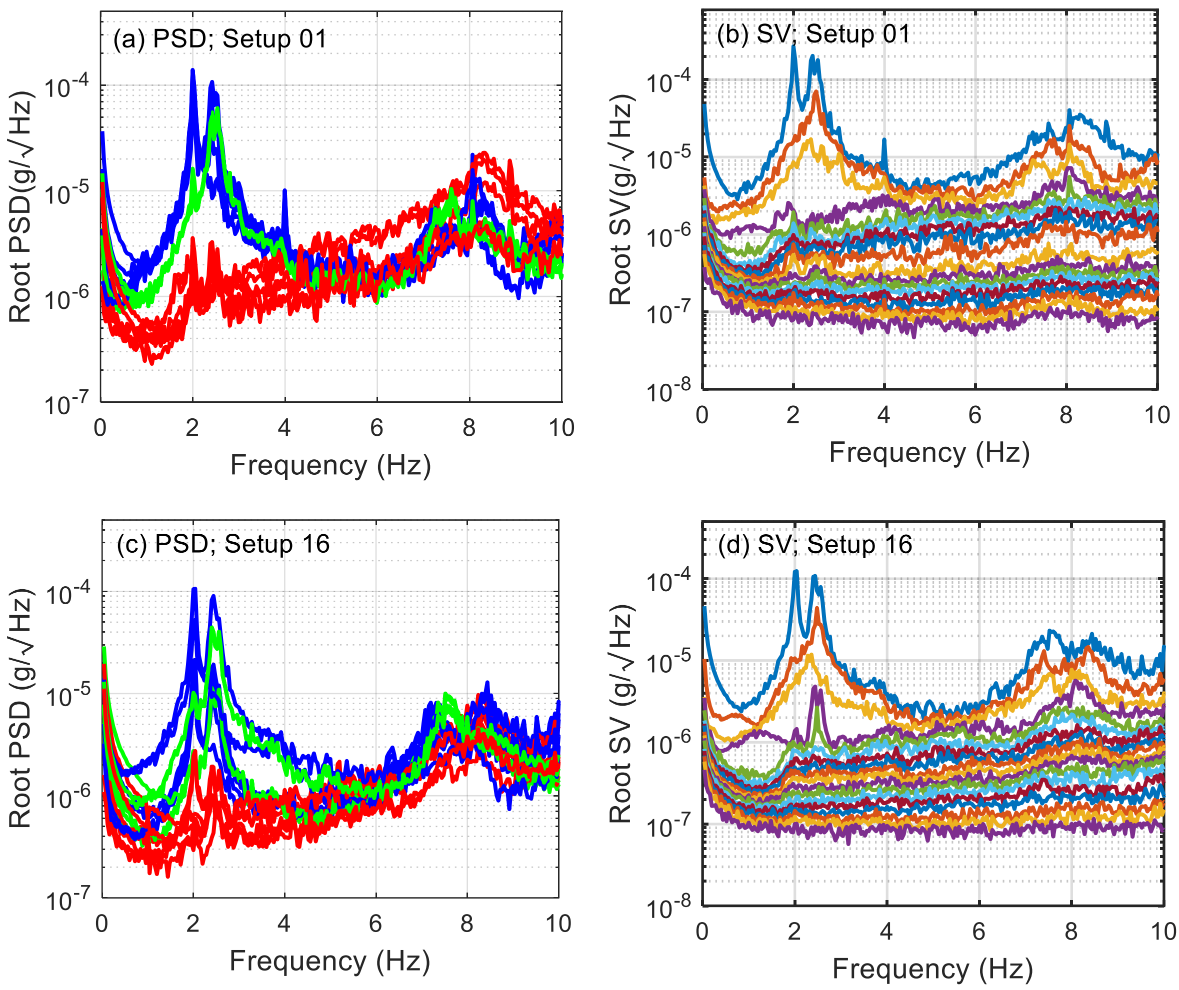

Figure 5 PSD and SV based on data in Setups 1 (the first testing day) and 16 (the second testing day). In PSD spectrum, blue line - x-axis; green line - y-axis; red line - z-axis.

As indicated in Figure 5(c) and (d), there are four modes in the region around 8 Hz, with much lower modal s/n ratios compared to the first three modes. Identification of these modes turns out to be challenging due to the poor-quality data on the first testing day. First, the PSD spectrum of Setup 1 in Figure 5(a) shows sharp peaks at 4, 8 and 8.87 Hz, which is also the case for other setups performed on the first testing day and which may have been due to harmonic excitation by machinery operating at a construction site near the building on the first testing day. While the harmonic signal at 4 Hz does not affect the identification of the modes because it is outside the resonant bands of modes of interest, special attention needs to be paid to the harmonic signals at 8 and 8.87 Hz, which are within the region of the modes. In BAYOMA, the FFTs within the (hand-picked) selected frequency band covering the modes of interest will be used to infer the modal parameters. To mitigate the influence of the harmonic signals, the FFTs at or near the harmonic signals should be excluded from the selected band otherwise they may introduce significant modelling errors with respect to the assumption of band-limited white noise excitations. Table 2 shows the selected frequency bands and initial guesses in the first setup data, which were manually selected based on the peaks observed in the SV spectrum.

Table 2 Selected frequency bands in Setup 1.

Mode	1	Close modes {2,3}	4	5	Close modes {6, 7}
Frequency band (Hz)	[1.87, 2.14]	[2.29, 2.65]	[6.95, 7.32]	[7.43,7.73]	[7.86, 9.03] excluding [8.02, 8.12] and [8.85, 8.91]
Initial guess (Hz)	2.01	{2.43, 2.52}	7.27	7.60	{8.17, 8.36}

A second challenging issue with the data collected on the first testing day is that the modes around 8 Hz are ‘buried’ by some vertical channels in Setups 1-6, as shown in Figure 5(a) where two red lines (Channels 6 and 9) obscure the blue and green peaks. This calls into question the validity of the i.i.d. noise assumption. On the other hand, direct identification of these modes based on the original data leads to a convergence problem. In view of these issues, an empirical method is developed here to 'pre-normalise' the data so that the processed data channels have practically a similar noise PSD level to allow the existing algorithms developed for i.i.d. noise [25,26] to be applied without the apparent risk of modelling error. Essentially, each channel of the original dataset is normalised by dividing it by the square root of its corresponding noise PSD, while the corresponding entries in the selection matrix are divided by the same value. To see why this works, consider a linear transformation $\hat{\ddot{\boldsymbol{x}}}_j^{(r)\prime} = \boldsymbol{R}^{(r)}\hat{\ddot{\boldsymbol{x}}}_j^{(r)}$, which transforms the original measured data $\left\{\hat{\ddot{\boldsymbol{x}}}_j^{(r)}\right\}$ in Setup r into a new set of data $\hat{\ddot{\boldsymbol{x}}}_j^{(r)\prime}$ through a $n_r \times n_r$ real invertible matrix $\boldsymbol{R}^{(r)}$. Correspondingly, the FFT and theoretical PSD of transformed data can be expressed by

$$\hat{\boldsymbol{\mathcal{F}}}_k^{(r)\prime} = \boldsymbol{R}^{(r)}\hat{\boldsymbol{\mathcal{F}}}_k^{(r)} = \boldsymbol{L}_r'\boldsymbol{\Phi}\,\boldsymbol{h}_k^{(r)}\boldsymbol{p}_k^{(r)} + \boldsymbol{R}^{(r)}\boldsymbol{\varepsilon}_k^{(r)} \tag{6}$$

$$\boldsymbol{E}_k^{(r)\prime} = \boldsymbol{L}_r'\boldsymbol{\Phi}\boldsymbol{H}_k^{(r)}\boldsymbol{\Phi}_r^{\mathrm{T}}\boldsymbol{L}_r'^{\boldsymbol{T}} + \boldsymbol{R}^{(r)}\boldsymbol{S}_e^{(r)}\boldsymbol{R}^{(r)T} \tag{7}$$

where $\boldsymbol{L}_r' = \boldsymbol{R}^{(r)}\boldsymbol{L}_r$; $\boldsymbol{S}_e^{(r)} = \boldsymbol{E}[\boldsymbol{\varepsilon}_k^{(r)}\boldsymbol{\varepsilon}_k^{(r)*}|\boldsymbol{\theta}]$ is the noise PSD matrix of the original data. If $\boldsymbol{R}^{(r)} = \left(S_{e0}^{(r)}\right)^{1/2}\left(\boldsymbol{S}_e^{(r)}\right)^{-1/2}$ where S_{e0} is an arbitrary reference value, then the noise PSD of new data reduces to $S_{e0}\boldsymbol{I}_n$, i.e., i.i.d. noise with common PSD. Consequently, Equation (7) takes the same form as (5). As a result, the theory and algorithms developed for the case of i.i.d. noise in Section 4 will apply (by replacing $\boldsymbol{L}_r$ with $\boldsymbol{L}_r'$). In implementation, $S_{e0}^{(r)}$ is chosen nominally by analyst and its choice does not affect the results [30]. The noise PSDs of data channels can be estimated empirically from data PSD spectrum or a huddle test [22].

Using data in Setup 1 as an example to demonstrate the proposed empirical method, from Figure 5(a), the data PSDs in Channels 6 and 9 are approximately twice as high as those of the remaining channels at frequencies away from the resonant region (e.g., 6 Hz, reflecting noise). To account for this disparity, the data in these two channels are divided by 2 so that the PSDs in these channels have a similar level as other channels. Accordingly, the corresponding entries in the selection matrix for Channels 6 and 9 become 0.5. Figure 6 shows the PSD and SV of the transformed data in Setup 1 where the modes around 8 Hz are more prominent in both PSD and SV spectra compared to the spectra based on the original data. A similar procedure applies to the data in Setups 2 – 6 and details are omitted here. Note that the transformed data are only used when identifying the modes around 8 Hz while the identification of the first three modes is based on the original data.

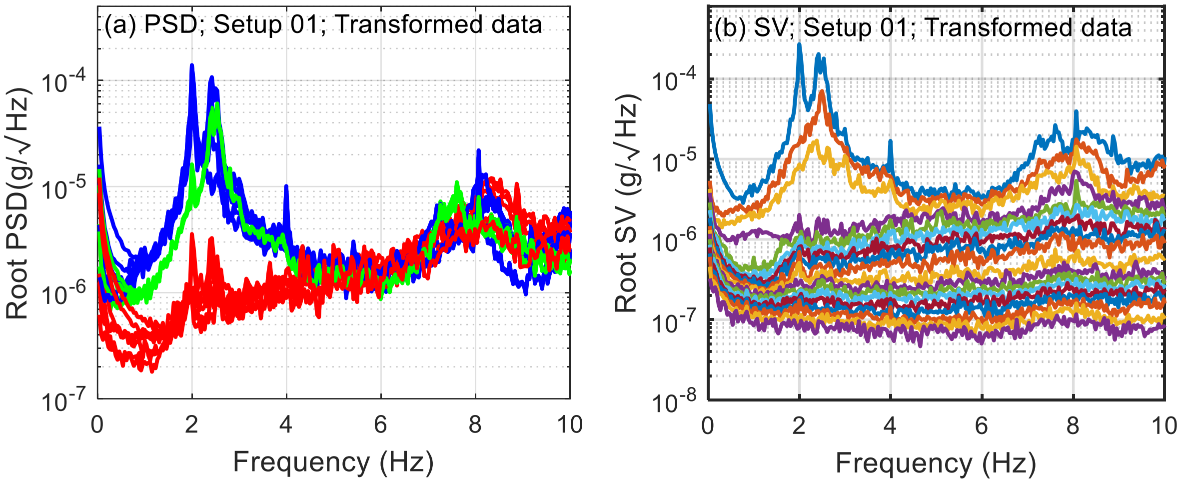

Figure 6 PSD and SV based on the transformed data in Setup 1. In PSD spectrum, blue line - x-axis; green line - y-axis; red line - z-axis.

5.2 Identified modes

Figure 7 shows the identified mode shapes of the first three modes, with sample means of the identified natural frequencies and damping ratios indicated in the figure. The value inside the parenthesis is the representative coefficient of variation (COV), which is attributed to both setup-setup variability and identification uncertainty [31]. The red and black lines represent the undeformed and deformed mode shapes, respectively. Mode 1 is dominated by the translational motion along the x-direction (i.e., weak direction). From the plan view, the building also rotates around the top of the figure. Modes 2 and 3 occur at close frequencies, being 2.42 Hz and 2.54 Hz, respectively and are both torsional modes. From the plan view, TPs located at the same in-plane positions on different floors exhibit nearly identical motion directions, indicating that the position of the centre of rotation is consistent across floors. To illustrate these modes more clearly, Figure 8 presents the plan views of Modes 2 and 3 on Level 10. It can be observed that the centre of rotation in Mode 2 is located on the left side of the figure, while in Mode 3 it is on the right.

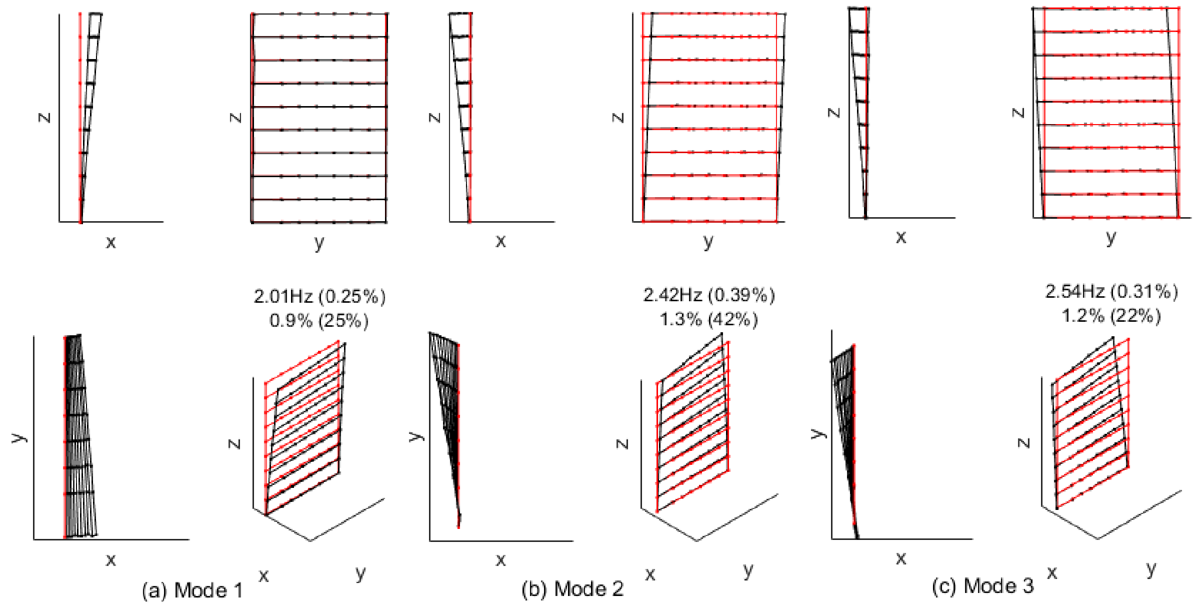

Figure 7 Identified mode shapes; Modes 1 – 3.

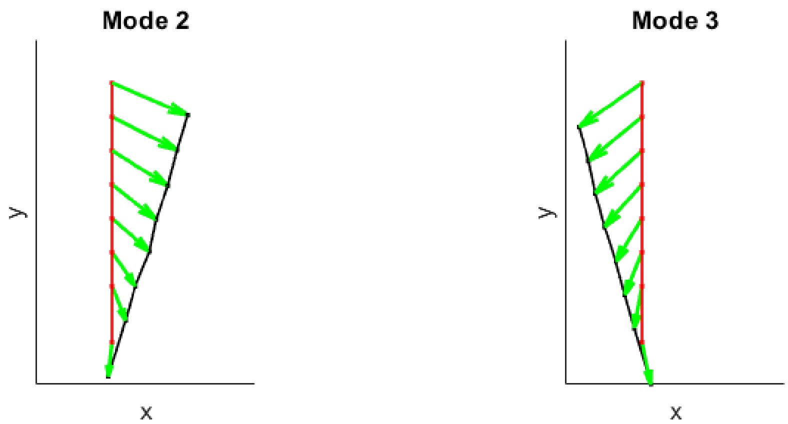

Figure 8 Plan view of Modes 2 and 3 on Level 10.

As discussed in the last section, Modes 4 – 7 are challenging to identify because the modes are buried by vertical signals (see Figure 5(a)) and harmonic excitations appear within the resonant bands but are interesting due to their vertical components. The signals in Setups 1-6 were first pre-normalised before modal identification. Figure 9 and Figure 10 show the mode shapes of Modes 4-7. Mode 4 is the second translational mode, which involves the motion along both the weak (x-) and strong (y-) directions, while Mode 5 is the second translational mode mainly along the y-direction. Mode 6 mainly involves the motion along the horizontal direction. It is seen that TPs at the stairwell in Mode 6 have much larger response compared to those in the lift core, especially at the lower levels. Mode 7 is a global vertical mode in the sense of having clear vertical motion at the lift core and stairwell and has relatively high damping ratio of 3.9%, but Modes 4-6 also have significant vertical motion along the connecting corridor with forms that resemble out of plane bending of a floor slab. Additionally, the vertical motion along the corridor for Modes 4-7 and at the lift core and stairwell for Mode 7 generally increases with floor height.

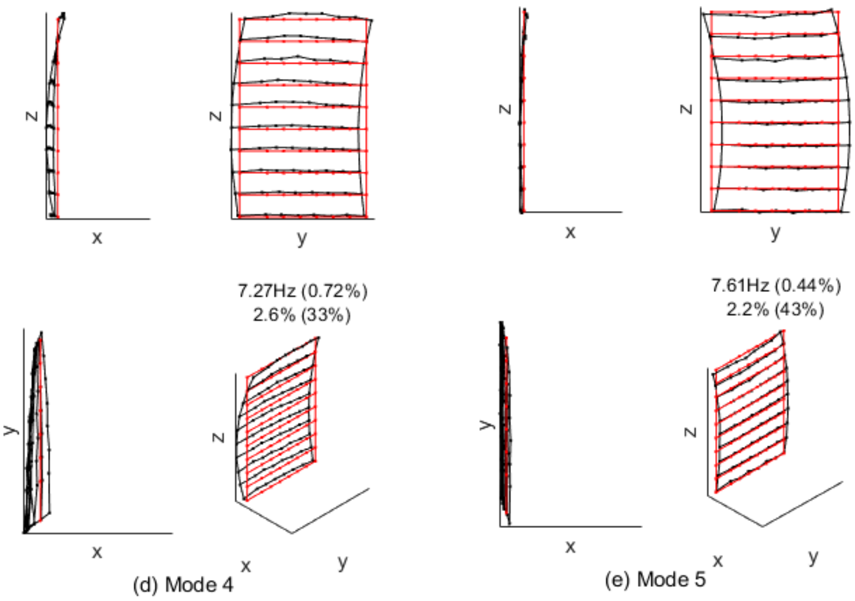

Figure 9 Identified mode shapes; Modes 4 – 5.

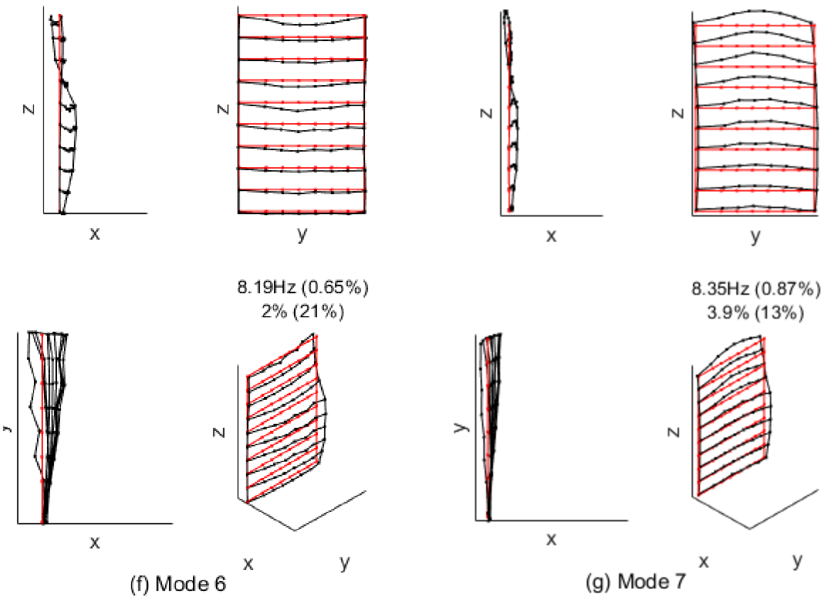

Figure 10 Identified mode shapes; Modes 6 – 7.

The appearance of modes with significant vertical motion in the higher range of frequencies prompted an investigation into vertical mode above the originally selected 10 Hz limit. A global vertical mode appearing at 11 Hz was identified with a damping ratio of 6.3%. The mode shape is shown in Figure 11 and is characterised by a rocking motion about the middle line with lift core and stairwell motion in antiphase. The lift core has a higher response compared to the stairwell. Similar to Modes 4-7, the vertical motion increases with floor height.

These modes were all that could be reliably identified from the ambient vibration data. In theory any structure has an infinite number of modes although for practical purposes in wind and seismic design of buildings only the first few modes involving horizontal sway and torsion are relevant. While not a safety issue, lightweight floor designs with low embodied carbon have enhanced concerns with vibration serviceability and driven requirements for identification of vertical vibration modes local to a specific floor [32] that have in some cases indicated vibration modes linking multiple floors, a phenomenon that occasionally has significant consequences [14]. What is particularly interesting about the study reported here is that it provided direct evidence linking vertical modes with global sway modes, although the ability to identify a much larger set is limited by the instrumentation (for data acquisition at high spatial resolution) and nature of dynamic loads (to excite adequately modes in all axes).

It is of interest to see that the higher modes around 8 Hz and 11 Hz have relatively larger damping ratios compared to the lower modes around 2 Hz. This observation aligns with the findings reported in [33], which investigated the dynamic responses of 24 buildings during earthquake events using an input-output identification technique to estimate damping ratios. There have been attempts to rationalise the origin of damping in buildings [34] but the underlying physical explanations for the trend observed here remain an open question.

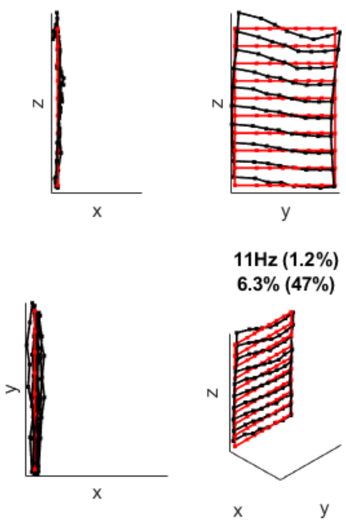

Figure 11 Identified mode shapes; Mode 8.

Table 3 summarises the averaged posterior COV among setups and sample COV (sample standard deviation among the setups divided by the sample mean of MPVs) of natural frequencies and damping ratios. The sample COV is affected not only by identification uncertainty but also by the variability of the modal parameters among different setups. For this reason, the sample COV is generally higher than the posterior COV. Both the posterior and sample COV are small for natural frequency, indicating a high identification precision. The posterior COVs of damping ratios are around 10% while the sample COVs range from 10% to 40%.

Table 3 Statistics of the identified natural frequencies and damping ratios.

Modal parameters		Mode							
		1	2	3	4	5	6	7	8
f	COV (%)	0.12	0.13	0.13	0.34	0.24	0.12	0.2	0.5
	Sample COV (%)	0.22	0.37	0.28	0.56	0.33	0.63	0.85	1
ζ	COV (%)	15	12	12	16	19	7	7	15
	Sample COV (%)	19	40	19	28	35	20	11	43

6 Long-term monitoring of dynamic properties

Following the multiple-setup test, one sensor was left in a secure room located at the southeast corner of the top floor (see Figure 3). Continuous data were collected over two months, from 9 December 2018 to 9 February 2019 during which time several strong wind events occurred, with maximum wind speeds exceeding 20 m/s. These include Storm Deirdre on 15 December 2018, a strong wind event on 27 January 2019, and Storm Erik, which lasted from 7 to 9 February 2019. In this section, the dynamic properties of the first three modes are investigated based on the monitoring data.

Conventionally, to track the temporal variation of modal parameters, data are first empirically divided into non-overlapping segments of equal length, and the modal parameters are identified within each segment using a time-invariant model. Potential time-varying behaviour is investigated based on the variation of the identified parameters across successive segments. For simplicity, the segment length is often assumed to be constant. However, intuitively, when the parameters exhibit significant changes (e.g., during a strong wind event), shorter segments should be used to reduce modelling errors against time-invariant properties and to improve temporal resolution. Conversely, during periods with little change in modal parameters, longer segments are preferable to improve identification precision. Motivated by the aforementioned issues, a Bayesian dynamic programming approach has been recently developed [21], which allows the data segment lengths to be adapted during the tracking based on the data acquired so far. From a Bayesian model class selection perspective, the 'optimal partitioning' of data, between which a change of modal parameters occurs, and the associated piecewise-constant modal properties are determined by maximising the probabilistic evidence supported by data. In this section, we use the Bayesian dynamic programming method to track the modal properties. In the approach, the length of the 'unit segment' needs to be defined first. It refers to the shortest time-invariant segment within which the modal parameters can still be uniquely determined. In this work, the unit segment length is set to 10 minutes, consistent with the data duration used in the multiple-setup test.

Figure 12 shows the tracking results of the first mode over the whole monitoring period, which are reported with black boxes covering the identified MPV ± 2 standard deviation range calculated using the data within the segment. The estimates of natural frequencies are in the interval 1.96 Hz to 2.06 Hz, a range of over 4.8%. The posterior uncertainty in natural frequencies is less than 1% while the posterior uncertainties in damping ratios and modal force PSDs are significantly higher, usually in the order of tens percent. The estimates of damping ratios range from 0.25% to 3.71%. The estimates of modal force PSD, which reflect the vibration level of the structure, generally exhibit diurnal variation and reach the local maxima at midday. The wind speed is also plotted in the figure for comparison [35], which ranges from 0 m/s to 22 m/s. A clear positive correlation between the modal force PSD and wind speed can be observed during strong wind events. To further investigate the variation of modal properties in strong wind events, Figure 13 shows the results during Storm Erik on 7 February 2019. During that day, the wind speed increased from 4 m/s at midnight to a peak of 18 m/s at 8 am, before gradually returning to 4 m/s by the end of the day. The modal force PSD shows a similar trend as the wind speed, increasing from 10^{-14} g^2/Hz to 10^{-10} g^2/Hz and then returning back to 10^{-14} g^2/Hz. In the meantime, the natural frequency shows a negative correlation with the vibration amplitude, decreasing from 2.01 Hz to 1.95 Hz and then returning to 2.01 Hz at the end of the day. The damping ratio increased from 0.6% to around 3% and then decreased to the original level. The potential amplitude dependence of natural frequencies and damping ratios will be investigated later. From Figure 13, when there is little change in the modal parameters (say, before 5 am), longer segments are selected for modal identification, giving a smaller identification uncertainty. Conversely, during the main event (say, between 6 am and 10 am), shorter segments are used to improve the temporal resolution. This is the potential advantage of using Bayesian dynamic programming for the tracking, in which the data segment lengths can adaptively adjust, justified by the Bayesian evidence.

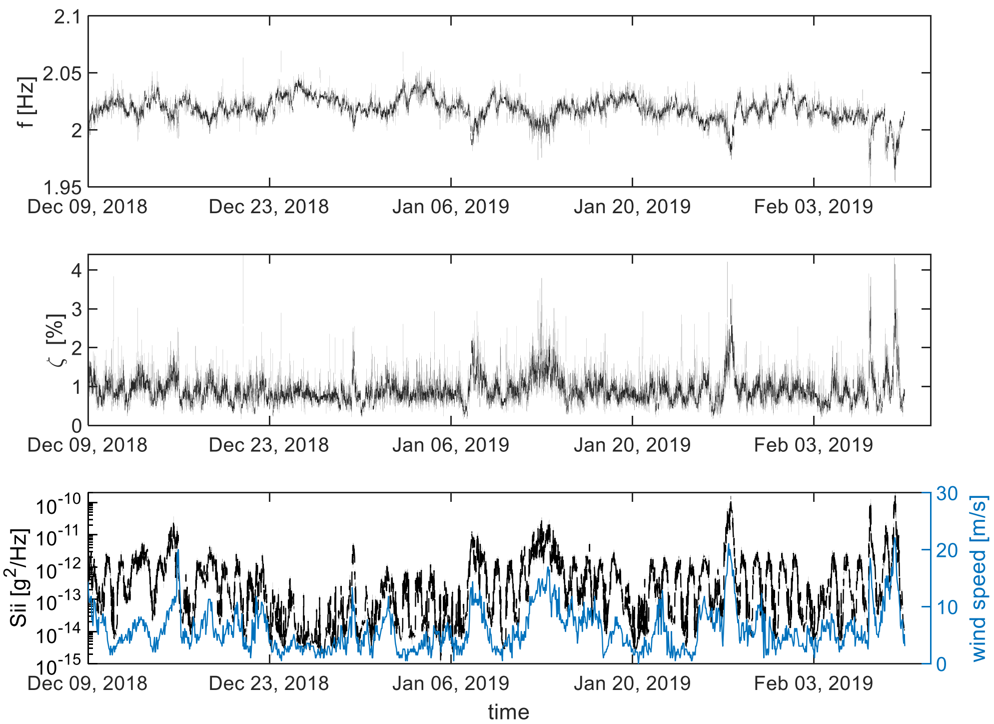

Figure 12 Tracking results of modal properties over the complete monitoring period; Mode 1; black box - identified MPV ± 2 standard deviation calculated using the data within the segment.

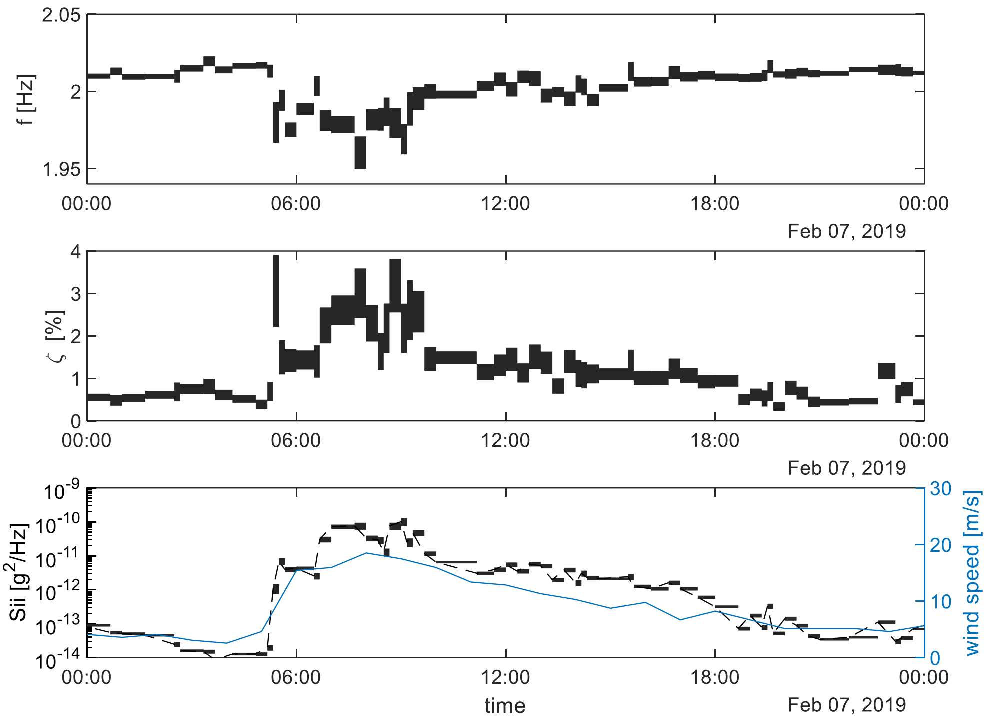

Figure 13 Tracking results of modal properties during Storm Erik; Mode 1; same legend as Figure 12.

Figure 14 shows the tracking results of closely spaced Modes 2 (black boxes) and 3 (red boxes). The identified natural frequencies and modal force PSDs exhibit generally similar trends for these two modes. However, the damping ratio of Mode 2 shows a larger variation compared to that of Mode 3 during some quiet periods. For example, Figure 15 shows the results between 12 and 15 December 2018, a quiet period with the wind speed around 5 m/s. It is seen that the damping ratio of Mode 2 changed significantly between 1% and 4% while that of Mode 3 remained relatively stable (around 1%).

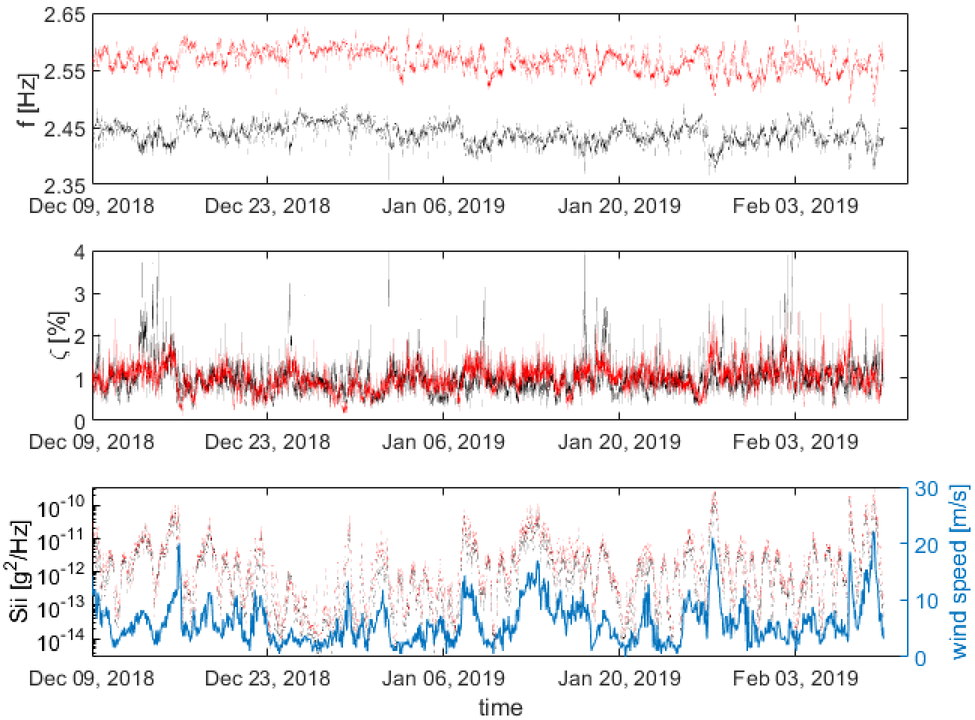

Figure 14 Tracking results of modal properties over the complete monitoring period; Modes 2 (black) and 3 (red); same legend as Figure 12.

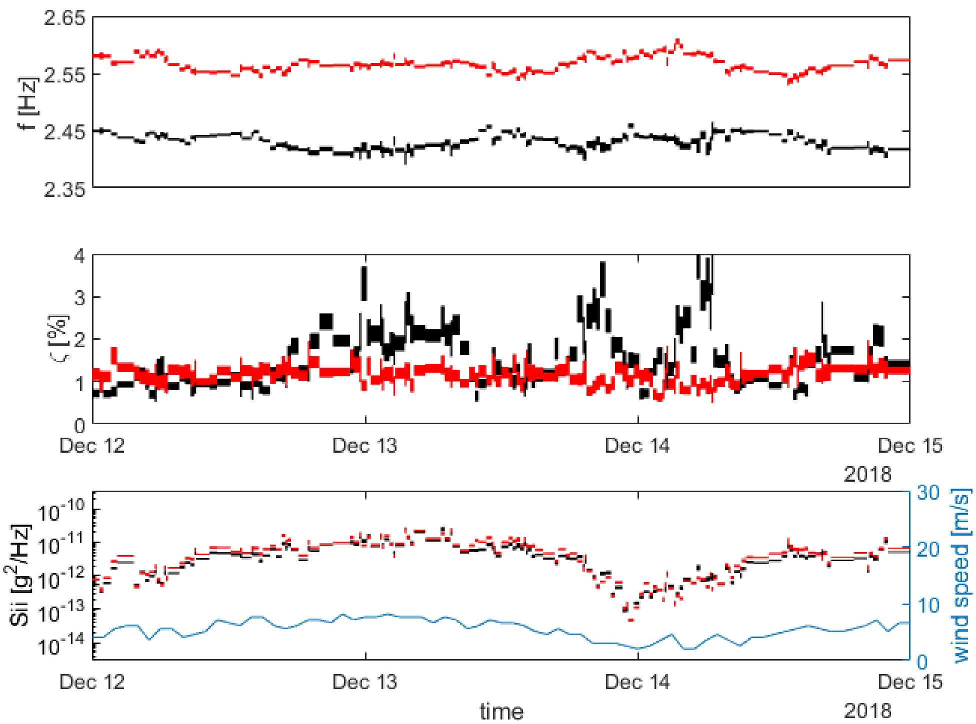

Figure 15 Tracking results of modal properties between 12 and 15 December 2018; Modes 2 (black) and 3 (red); same legend as Figure 12.

The potential amplitude dependence of modal parameters has been investigated. Figure 16 shows the identified natural frequency and damping ratio versus modal force PSD for Mode 1. The results are reported with a dot at the MPV and an error bar indicating ± 2 posterior standard deviation. There is an inverse correlation between the natural frequency and modal force PSD, especially at higher vibration levels. A clear positive trend can be observed between the damping ratio and modal force PSD for Mode 1. Figure 17 shows the identified natural frequency versus modal force PSD for Modes 2 and 3. Similar to Mode 1, the natural frequency shows a decreasing trend with modal force PSD for both modes. One potential explanation for the negative correlation is the progressive loosening of frictional joints at higher vibration amplitudes, which can lead to a reduction in global stiffness and, consequently, a decrease in natural frequencies [36]. The correlation between the damping ratio and modal force PSD is less obvious for these two modes. When the modal force PSD is around $10^{-12}\ \mathrm{g}^2\ /\ \mathrm{Hz}$, the estimates of damping ratios in Mode 2 changed significantly, which implies that the estimates are affected by other unknown factors. The damping ratios of Mode 3 remain relatively stable around 1%, regardless of the modal force PSD.

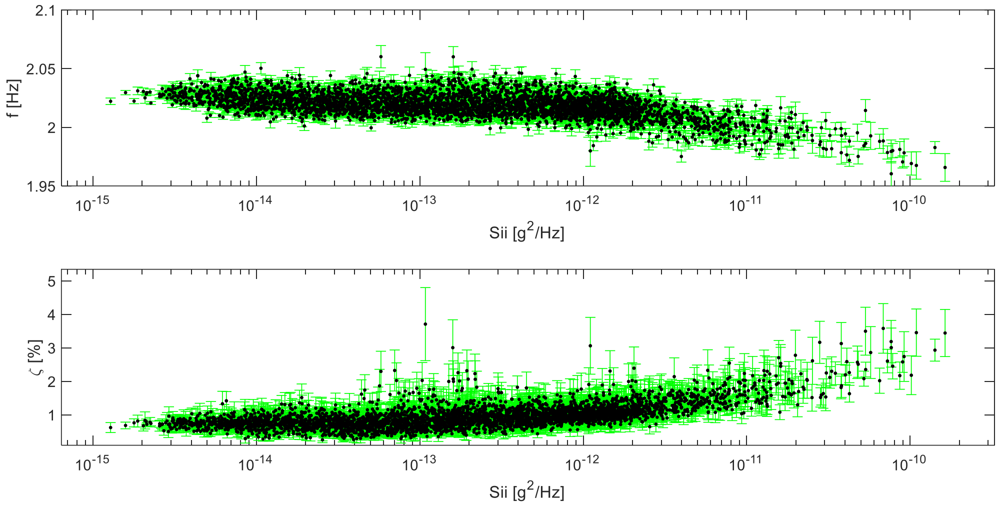

Figure 16 Identified natural frequency and damping ratio versus modal force PSD; Mode 1.

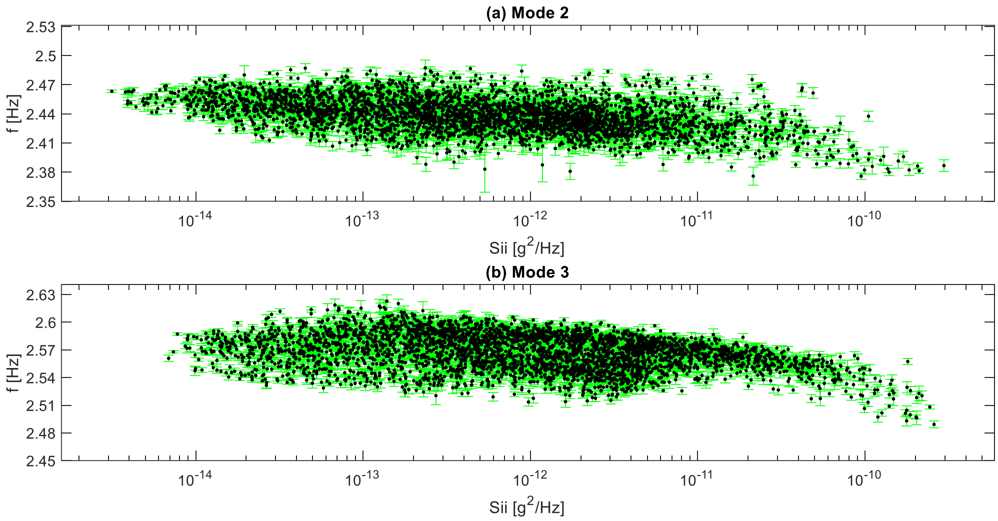

Figure 17 Identified natural frequency versus modal force PSD; Modes 2 and 3.

Using the results obtained during the monitoring period, a probability model to predict the distribution of modal parameters in the future is established based on the theory developed in [31]. Here, we assume that the data collected during the monitoring period is rich enough to cover a future scenario in the sense that in a future time window, the environment corresponds to the past time windows in Figure 12 and Figure 14. The modal parameter is modelled to have value in one of the data segments with the probability w_i proportional to the duration of data segment. In the above context, the PDF of modal parameter θ can be modelled by

$$p_{\Theta}(\theta|D) = \sum_{i=1}^{N_s} \frac{w_i}{\sqrt{2\pi\hat{c}_i}} \exp\left[-\frac{1}{2\hat{c}_i}\left(\theta - \hat{\theta}_i\right)^2\right] \tag{8}$$

where N_s is the number of partitioned segments; $w_i = N_{ui} / N_u$ where N_{ui} is the number of unit segments contained in the $i-th$ partitioned segment while N_u is the total number of unit segments over the monitoring period; $\hat{\theta}_i$ and $\hat{c}_i$ are the posterior MPV and variance identified based on the $i-th$ partitioned segment data, respectively. It can be shown that the expectation μ and variance c of θ are given by

$$\mu = \sum_{i=1}^{N_s} w_i \hat{\theta}_i \qquad c = \sum_{i=1}^{N_s} w_i (\hat{\theta}_i - \mu)^2 + \sum_{i=1}^{N_s} w_i \hat{c}_i \tag{9}$$

The expectation is the weighted mean of posterior MPVs among the data segments. The variance is the sum of the weighted sample variance among the segments (reflecting the variability of modal parameters) and the weighted mean of the posterior variances (reflecting the identification uncertainty). Figure 18 shows the PDF of natural frequencies and damping ratios of Modes 1-3. The mean and COV of the distribution are shown above each subfigure. The distributions are roughly Gaussian with a unique peak around the mean value. The mean values for all the damping ratios are around 1%. The COVs of natural frequencies are below 1% while the COVs of damping ratios range from 29% to 40%. The predicted distribution has the potential to be used for anomaly detection when new data is acquired in the future.

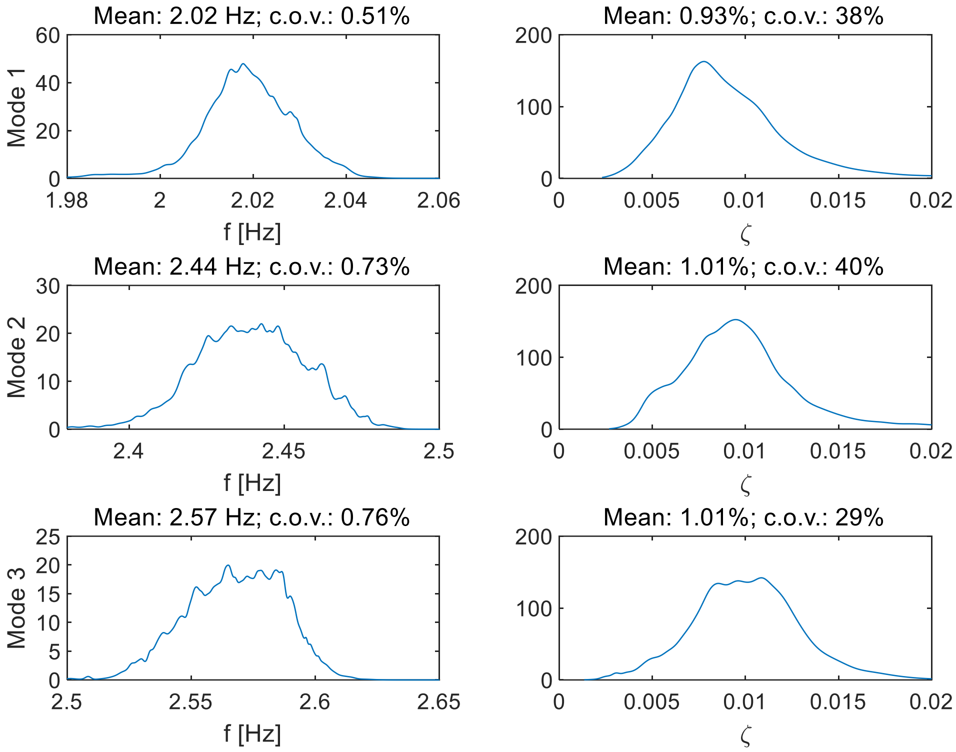

Figure 18 Predicted PDF of modal parameters.

7 Conclusions

This paper has presented the work on a full-scale vibration test of a mid-rise building and modal identification using a multiple-setup BAYOMA algorithm. Eight modes have been identified, mainly concentrated in two frequency ranges, around 2 Hz and 8 Hz, respectively. The first mode is a combination of translational mode along the weak direction and torsional mode. Both the second and third modes are torsional, occurring at very close frequencies. The damping ratios of lower modes around 2 Hz are around 1% while the higher modes around 8 Hz have relatively larger damping ratios, above 2%. The higher frequency set of modes exhibit significant vertical components, with modes at 8.35 Hz and 11 Hz having significant vertical response in the axially stiffer stairwell and lift core and being associated with high damping ratios of 3.9% and 6.3%.

The measured vibration data were contaminated by harmonic signals in the resonant bands around 8 Hz. As a frequency domain method, BAYOMA makes use of the FFTs within the (hand-picked) frequency bands for inference and the bands need not be continuous. As a result, BAYOMA can still apply to such datasets by excluding the FFTs at or near the harmonic signals from the selected bands. The noise disparity and buried modes lead to challenges in the modal identification. The data were pre-normalised through a linear transformation to allow the existing algorithms developed for i.i.d. noise to be applied without the apparent risk of modelling error. The identified modes based on the processed data are physically reasonable.

The structural modal properties have been tracked over two months by a recently developed Bayesian dynamic programming method. Regardless of modes, there is a significant negative correlation between natural frequencies and vibration levels, especially during strong winds. The damping ratio of the first mode shows a clear positive trend with modal force PSD, increasing from less than 1% to 4%. The relationship is less clear for the second and third modes due to the significant scatters. A probabilistic model has been established to predict modal parameters using the monitoring data. The COV of natural frequency in the model is less than 1% while that of damping ratios are in the order of tens of percent. The model has the potential to be used in anomaly detection when new data are acquired in the future.

8 Acknowledgements

This work is funded by the UK Engineering & Physical Sciences Research Council through the BAYOMALAW project (Grant EP/N017897/1) and the ROSEHIPS project (Grant EP/W005816/1). The fourth author gratefully acknowledges the support of the National Natural Science Foundation of China (52308320), National Key R&D Program of China (2022YFB2603300), and Shenzhen Science and Technology Program (JCYJ20220818095608018). The majority of the work was performed during the PhD study of the first author at the University of Liverpool; see the thesis in [37]. Any opinions, findings and conclusions or recommendations expressed in this material are those of the authors and do not reflect the views of the funders. We are grateful to Dr Tao Yin, Miss Ningxin Weng, Mr Zixuan Liu, Mr Junyuan Chen and Mr C.Y. Liu from the University of Liverpool for assisting with the field test.

9 Data availability

The field data in this study will be archived in an open repository for public access.

10 Ethics Declarations

Conflict of Interest: the fifth author James Brownjohn serves as associate editor in the Journal of Civil Structural Health Monitoring.

11 References

[1] Jafari M, Alipour A. Methodologies to mitigate wind-induced vibration of tall buildings: A state-of-the-art review. Journal of Building Engineering 2021;33:101582. https://doi.org/10.1016/j.jobe.2020.101582.

[2] Lam HF, Fu ZY, Adeagbo MO, Yang JH. Time-domain structural model updating following the Bayesian approach in the absence of system input information. Eng Struct 2024;314:118321. https://doi.org/10.1016/j.engstruct.2024.118321.

[3] Yin T, Jiang QH, Yuen KV. Vibration-based damage detection for structural connections using incomplete modal data by Bayesian approach and model reduction technique. Eng Struct 2017;132:260–77. https://doi.org/10.1016/j.engstruct.2016.11.035.

[4] Zhang FL, Yang YP, Xiong HB, Yang JH, Yu Z. Structural health monitoring of a 250-m super-tall building and operational modal analysis using the fast Bayesian FFT method. Struct Control Health Monit 2019;26. https://doi.org/10.1002/stc.2383.

[5] Cross EJ, Koo KY, Brownjohn JMW, Worden K. Long-term monitoring and data analysis of the Tamar Bridge. Mech Syst Signal Process 2013;35:16–34. https://doi.org/10.1016/j.ymssp.2012.08.026.

[6] Ni Y-C, Zhang Q-W, Liu J-F. Dynamic performance investigation of a long-span suspension bridge using a Bayesian approach. Mech Syst Signal Process 2022;168:108700. https://doi.org/10.1016/j.ymssp.2021.108700.

[7] Pan H, Jiang F, Wu J, Deng T, Fu J. Bayesian operational modal analysis of two supertall buildings under Super Typhoon Saola. Eng Struct 2025;330. https://doi.org/10.1016/j.engstruct.2025.119907.

[8] Brownjohn JMW, Raby A, Au S-K, Zhu Z, Wang X, Antonini A, et al. Bayesian operational modal analysis of offshore rock lighthouses: Close modes, alignment, symmetry and uncertainty. Mech Syst Signal Process 2019;133. https://doi.org/10.1016/j.ymssp.2019.106306.

[9] Jimenez Capilla JA, Au SK, Brownjohn JMW, Hudson E. Ambient vibration testing and operational modal analysis of monopole telecoms structures. J Civ Struct Health Monit 2021;11:1077–91. https://doi.org/10.1007/s13349-021-00499-4.

[10] Song M, Partovi Mehr N, Moaveni B, Hines E, Ebrahimian H, Bajric A. One year monitoring of an offshore wind turbine: Variability of modal parameters to ambient and operational conditions. Eng Struct 2023;297. https://doi.org/10.1016/j.engstruct.2023.117022.

[11] Brownjohn J, Racic V, Chen J. Universal response spectrum procedure for predicting walking-induced floor vibration. Mech Syst Signal Process 2016;70–71:741–55. https://doi.org/10.1016/j.ymssp.2015.09.010.

[12] Yuan Y, Gao Z, He L, Lei Z. Research on the Vibration Response of High-Rise Buildings under Blasting Load. Mathematics 2024;12. https://doi.org/10.3390/math12203165.

[13] Vela V, Taciroglu E, Kohler M. Vertical System Identification of a 52-Story High-Rise Building Using Seismic Accelerations. Structural Health Monitoring 2023: Designing SHM for Sustainability, Maintainability, and Reliability - Proceedings of the 14th International Workshop on Structural Health Monitoring 2023:2992–3000. https://doi.org/10.12783/shm2023/37076.

[14] Lee SH, Lee KK, Woo SS, Cho SH. Global vertical mode vibrations due to human group rhythmic movement in a 39 story building structure. Eng Struct 2013;57:296–305. https://doi.org/10.1016/j.engstruct.2013.09.035.

[15] Pan H, Au SK, Fu J, Xu A, He Y. Field measurement and wind tunnel experimental investigation of a supertall building with closely spaced modes under typhoon Mangkhut. Journal of Wind Engineering and Industrial Aerodynamics 2022;226. https://doi.org/10.1016/j.jweia.2022.105033.

[16] Zhou K, Li Q-S, Li X. Dynamic Behavior of Supertall Building with Active Control System during Super Typhoon Mangkhut. Journal of Structural Engineering 2020;146:4020077. https://doi.org/10.1061/(asce)st.1943-541x.0002626.

[17] He Y, Liu Y, Wu M, Fu J, He Y. Amplitude dependence of natural frequency and damping ratio for 5 supertall buildings with moderate-to-strong typhoon-induced vibrations. Journal of Building Engineering 2023;78:107589. https://doi.org/10.1016/j.jobe.2023.107589.

[18] Satake N, Suda K, Arakawa T, Sasaki A, Tamura Y. Damping Evaluation Using Full-Scale Data of Buildings in Japan. Journal of Structural Engineering 2003;129:470–7. https://doi.org/10.1061/(asce)0733-9445(2003)129:4(470).

[19] Ha T, Shin SH, Kim H. Damping and natural period evaluation of tall RC buildings using full-scale data in Korea. Applied Sciences (Switzerland) 2020;10. https://doi.org/10.3390/app10051568.

[20] Wang JT, Jin F, Zhang CH. Estimation error of the half-power bandwidth method in identifying damping for multi-DOF systems. Soil Dynamics and Earthquake Engineering 2012;39:138–42. https://doi.org/10.1016/j.soildyn.2012.02.008.

[21] Yang Y, Zhu Z, Au SK. Bayesian dynamic programming approach for tracking time-varying model properties in SHM. Mech Syst Signal Process 2023;185:109735. https://doi.org/10.1016/j.ymssp.2022.109735.

[22] Zhu Z, Au SK, Wang X. Instrument noise calibration with arbitrary sensor orientations. Mech Syst Signal Process 2019;117:879–92. https://doi.org/10.1016/j.ymssp.2018.07.052.

[23] Au SK, Brownjohn JMW, Mottershead JE. Quantifying and managing uncertainty in operational modal analysis. Mech Syst Signal Process 2018;102:139–57. https://doi.org/10.1016/j.ymssp.2017.09.017.

[24] Reynders E. System Identification Methods for (Operational) Modal Analysis: Review and Comparison. Archives of Computational Methods in Engineering 2012;19:51–124. https://doi.org/10.1007/s11831-012-9069-x.

[25] Zhu Z, Au SK, Li B, Xie YL. Bayesian operational modal analysis with multiple setups and multiple (possibly close) modes. Mech Syst Signal Process 2021;150. https://doi.org/10.1016/j.ymssp.2020.107261.

[26] Zhu Z, Au SK. Uncertainty quantification in Bayesian operational modal analysis with multiple modes and multiple setups. Mech Syst Signal Process 2022;164. https://doi.org/10.1016/j.ymssp.2021.108205.

[27] Au SK. Operational modal analysis: Modeling, bayesian inference, uncertainty laws. 2017. https://doi.org/10.1007/978-981-10-4118-1.

[28] Li B, Wang P, Zhu Z, Li Z, Xiao Y. Ambient Vibration Test and Retest of a Multistory Factory Building. Journal of Performance of Constructed Facilities 2024;38:1–13. https://doi.org/10.1061/jpcfev.cfeng-4662.

[29] Zhu Z, Au SK, Brownjohn J, Koo KY, Nagayama T, Bassitt J. Uncertainty quantification of modal properties of Rainbow Bridge from multiple-setup OMA data. Eng Struct 2025;330:119901. https://doi.org/10.1016/j.engstruct.2025.119901.

[30] Ma X, Zhu Z, Au SK. Treatment and effect of noise modelling in Bayesian operational modal analysis. Mech Syst Signal Process 2023;186. https://doi.org/10.1016/j.ymssp.2022.109776.

[31] Zhang FL, Au SK. Probabilistic Model for Modal Properties Based on Operational Modal Analysis. ASCE ASME J Risk Uncertain Eng Syst A Civ Eng 2016;2:1–12. https://doi.org/10.1061/AJRUA6.0000843.

[32] Pavic A, Reynolds P. Experimental assessment of vibration serviceability of existing office floors under human-induced excitation. Exp Tech 1999;23:41–5. https://doi.org/10.1111/j.1747-1567.1999.tb01305.x.

[33] Cruz C, Miranda E. Evaluation of the Rayleigh damping model for buildings. Eng Struct 2017;138:324–36. https://doi.org/10.1016/j.engstruct.2017.02.001.

[34] Jeary AP. Damping in structures. Journal of Wind Engineering and Industrial Aerodynamics 1997;72:345–55. https://doi.org/10.1016/S0167-6105(97)00263-8.

[35] Met Office. MIDAS Open: UK hourly weather observation data, v202407. NERC EDS Centre for Environmental Data Analysis 2024. https://doi.org/https://dx.doi.org/10.5285/c50776e4903942cdb329589da70b83fe.

[36] Au SK, Zhang FL, To P. Field observations on modal properties of two tall buildings under strong wind. Journal of Wind Engineering and Industrial Aerodynamics 2012;101:12–23. https://doi.org/10.1016/j.jweia.2011.12.002.

[37] Zhu Z. Bayesian Operational Modal Analysis with Multiple Setups and Multiple Modes 2020.